Article

Study on Residual Oil Distribution Law during the Depletion Production and Water Flooding Stages in the Fault-Karst Carbonate Reservoirs

Bochao Tang [1], Ke Ren [1], Haitao Lu [1], Chenggang Li [1], Chunying Geng [1], Linshan Wei [1], Zhenhan Chai [1] and Shouya Wu [2,*]

[1] Sinopec Northwest Oilfield Company, Urumqi 830011, China
[2] Key Laboratory of In-Situ Property-Improving Mining of Ministry of Education, Taiyuan University of Technology, Taiyuan 030024, China
* Correspondence: wushouya@tyut.edu.cn

Abstract: The fault-karst carbonate reservoir is a new type of deep carbonate oil and gas resource and a target for exploration and development. The distribution of remaining oil in this kind of oilfield is very complicated because of its unique reservoir characteristics of vertical migration and accumulation, segmented accumulation, and differential accumulation. Therefore, the S91 reservoir block, a typical fracture-vuggy carbonate reservoir in the Tahe oilfield, was taken as the object of this research. According to the development characteristics as well as the porosity and permeability characteristics of the fracture-vuggy, the reservoirs were divided into three types: cave, pore, and fracture. A numerical simulation model of the fracture-vuggy reservoir of the S91 unit was established, and the historical fitting accuracy with dynamic production data was more than 90%. Then, the distribution characteristics of the remaining oil in the depletion stage of the fault-karst carbonate reservoir were further studied and based on the analysis of the reservoir water-flood flow line, the remaining oil distribution characteristics in the depletion stage of the fault solution reservoir were revealed. The results show that the remaining oil distribution patterns during the depletion production stage can be divided into three types: attic type, bottom water coning type, bottom water running type. Due to the serious problem of the bottom aquifer lifting caused by the reservoir development, the residual oil between wells was relatively abundant during the depletion production stage. According to the simulation results, the remaining oil distribution modes in the water drive development stage were identified as three types: sweeping the middle between wells, bottom water connection and circulation, and oil separation through high-permeability channels. In addition, the reservoir connectivity was the main controlling factor for the remaining oil distribution in the fault-karst carbonate reservoir.

Keywords: residual oil distribution; fault-karst carbonate reservoirs; depletion production; water flooding

1. Introduction

In China, deep carbonate oil-gas resources are the hotspot of oil development, while fault-karst reservoirs are the major components of deep carbonate oil-gas resources [1–4]. Mainly controlled by the strike-slip fault zone from corrosion of different degrees, they have the characteristics of segmented accumulation, trans-layer migration, and interrupted spatial distribution along the fault zone [1,5]. Fault-karst reservoirs are new reservoir types in nature, having distinct characteristics for deep carbonate oil-gas exploration and exploitation in China [6–10]. The sizes of fractured-vuggy reservoirs in the fault-karst traps are mainly controlled by the transformation scale and corrosion strength of the strike-slip fault zone [11–13]. Generally, fractured-vuggy reservoirs with high quality are developed along the major fault zone, mostly presenting stripped distribution and local

decentralization patterns [13,14]. Development has demonstrated strong local stratum deformation at the tensile-separation and press-torsion sections of the strike-slip fault zone, mainly developing flower structures [15,16]. The reservoir space is dominated by large caves, which are the most developed parts of the fractured-vuggy reservoirs due to the wide fracture zone and the strong corrosion action [17]. Vertical fractures with high angles are mainly developed at the translation section, resulting in relatively narrowed development scales in the reservoirs. The development degree of fractured-vuggy reservoirs along the strike-slip fault zone presents obvious segmental features.

The accumulation characteristics of fault-karst reservoirs are not responsible for the location and height of regional unconformities and structures [18–21]. Hydrocarbon is accumulated vertically along the fault zone and migrates along the gap-net system in a T-shape, with vertical migration, segmental accumulation, and differential aggregation characteristics [22–24]. The hydrocarbon enrichment degree at the major fracture zone of the fault-karst reservoirs is high, resulting in high production rates [25]. In addition, the large and small fractures are characterized by the presence of large and small hydrocarbon production capacities, respectively, while zones with a lack of fractures are characterized by a lack of hydrocarbon reservoirs [26,27]. Different fault-karst reservoirs along the same fracture zone are characterized by segmental accumulation, differential enrichment, and different developmental features [28,29]. The size and connectivity of fault-karst segments control the distribution and scale of the reservoirs. The carbonate matrix is characterized by insignificant reservoir permeability. In addition, reservoir spaces have various shapes, great size disparities, uneven distributions, and strong heterogeneity, resulting in complex residual oil distributions in the developed oilfields [30]. Therefore, comprehensive studies on the residual oil distribution patterns and improvement of overall reservoir management are of practical significance for improving the development efficiency and ensuring effective residual oil exploitation.

Through many experiments and numerical simulations, several researchers have studied the distribution patterns of residual oil in fractured-vuggy carbonate reservoirs [31,32]. Rong et al. [9,33,34] classified the residual oil reservoir into four categories and five sub-categories based on the distribution features by analyzing the fine reservoir description and dynamic production test data. Li et al. [35] proposed extraction of the residual oil through circulating water, surfactant flooding, or gas from fractured buried hill reservoirs. Zheng and Yang et al. [33,36] carried out a systematic study on the multi-scale features of the reservoir space and types, as well as on the spatial patterns and distribution models of the fractured-vuggy bodies and their relationships with production wells based on well logging, core, earthquake, and production performance data. In addition, a model of effect factors influencing residual oil distribution after water flooding was established. To directly simulate and predict the development process of fractured porous reservoirs, Liu et al. [37] proposed methods for establishing a macroscopic model for fractured porous reservoirs, and provided some application examples. Because of the difference in the reservoir physical properties, some issues may exist, including water invasion and uncertain residual oil distributions, thereby resulting in a great challenge to water-flooding in carbonate reservoirs. Li et al. [35] carried out a 3D water-flooding experiment using inter-layer heterogeneous physical models and quantitatively characterized the water-flooding status, mode, and residual oil distribution in the porous carbonate reservoirs with bottom water. To sum up, the existing studies on residual oil distribution have been mainly focused on fractured reservoirs, while for fractured-vuggy reservoirs, the research has been focused on bottom aquifer drive using numerical simulations and physical experiments. Thus, systematic research on the residual oil distribution patterns in fault-karst carbonate reservoirs needs to be studied.

The S91 unit is a typical fractured-vuggy fault-karst carbonate reservoir, as in our previous studies [38], which has experienced natural energy and water flooding development stages since it was first exploited. Indeed, this unit is characterized by a recovery rate and moisture content of about 11.5 and 83%, respectively, indicating a high moisture content

and low recovery rate. In this context, the present study aims to simulate the residual oil distribution in the S91 unit of the fault-karst reservoirs during the depletion production stage. In addition, the residual oil distribution characteristics of the fault-karst reservoir during the water-flooding stage were investigated in this study by analyzing the flow line of the injected water. Therefore, this study aims to provide technical support for the efficient exploitation of fault-karst reservoirs.

2. Establishment of a Numerical Simulation Model for Fractured-Vuggy Fault-Karst Reservoirs

Based on the geological data of the S91 unit, a numerical simulation model of fractured-vuggy fault-karst reservoirs was built by dividing the reservoir types and assigning the corresponding porosity and permeability parameters, the relative permeability curves.

2.1. Establishment of a Numerical Simulation Model

In this study, the geological model of the S91 unit was obtained using Petrel 2014 software to classify the reservoir types and to establish a numerical simulation model for the S91 unit of the fractured-vuggy reservoir. According to the porosity and permeability characteristics in different areas of the reservoir, three reservoir types, caves, vugs, and fractures or faults, were determined. It should be noted that the porosity and permeability of matrixes are obtained in the laboratory, and the parameters of these reservoir types were adjusted by combing with well-logging data. The spatial distributions of the reservoir types are shown in Figure 1.

The partial grid model was obtained by superposing multi-reservoirs. Therefore, some of the porosity and permeability parameters of these grids were modified in this study. The permeability data were merged to determine the preferential migration passage, which is the maximum permeability value of the superimposed reservoir, while that of the porosity was the sum of directions. The porosity and permeability models involved in the numerical simulation were now established. The temperature, pressure, and physical property parameter data, as well as the relative permeability curves of the fractured-vuggy unit, were first determined (Table 1 and Figure 2), then a numerical simulation model of the typical fractured-vuggy S91 unit was established.

Table 1. Physical parameters of the numerical mode of the S91 unit.

Model Parameter	Value	Model Parameter	Value
Reservoir temperature	127 °C	Reservoir pressure	62 MPa
Rock compressibility	4.05×10^{-5} 1/MPa	Fluid compressibility	10.03×10^{-4} 1/MPa
Porosity	0–0.54	Permeability	5–1200 mD
Initial oil saturation	0.77	Reservoir depths	about 5000 m

2.2. History Matching and Model Validation

History matching involves adjusting the reservoir parameters to establish a model representing the real behavior of the reservoir as far as possible based on the production data. It is, therefore, a process of model validation. History matching plays an important part in the numerical simulation of simulating past reservoir data and comparing the data with the actual production data to establish a model representing the real behavior of reservoirs, to a certain extent through continuous parameter adjustments. Therefore, history matching can be considered a process of model validation, allowing predictions of reservoir production. In mathematics, history matching is an equation solved with multiple variables and multiple solutions. In other words, multiple parameters can be used to obtain the same production behavior. From a reservoir exploitation perspective, the history of reservoir exploitation is influenced by several geological, engineering, and production measure factors, making history matching a difficult numerical simulation task. The porosity and permeability of the S91 unit reservoir presented substantial differences.

Porosity can be adjusted using inverse solutions and statistical laws and revised by the inverse-fitting method. On the other hand, the theory for adjusting permeability has no unification. The permeability data can be revised when fitting the dynamic production.
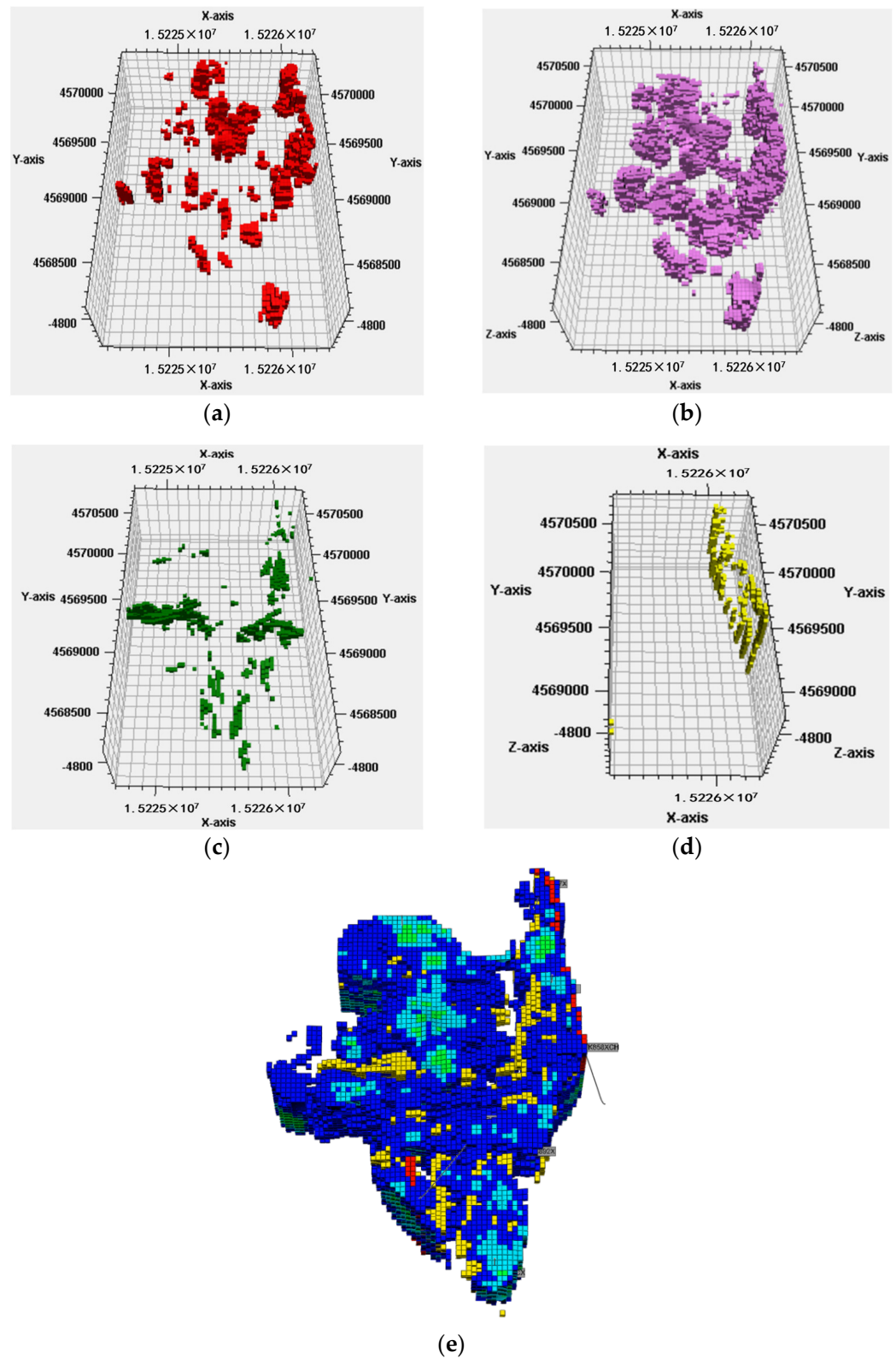

Figure 1. Reservoir distribution of the S91 unit. (**a**) Caves; (**b**) vugs; (**c**) fractures; (**d**) faults; (**e**) reservoir model of the S91 unit.
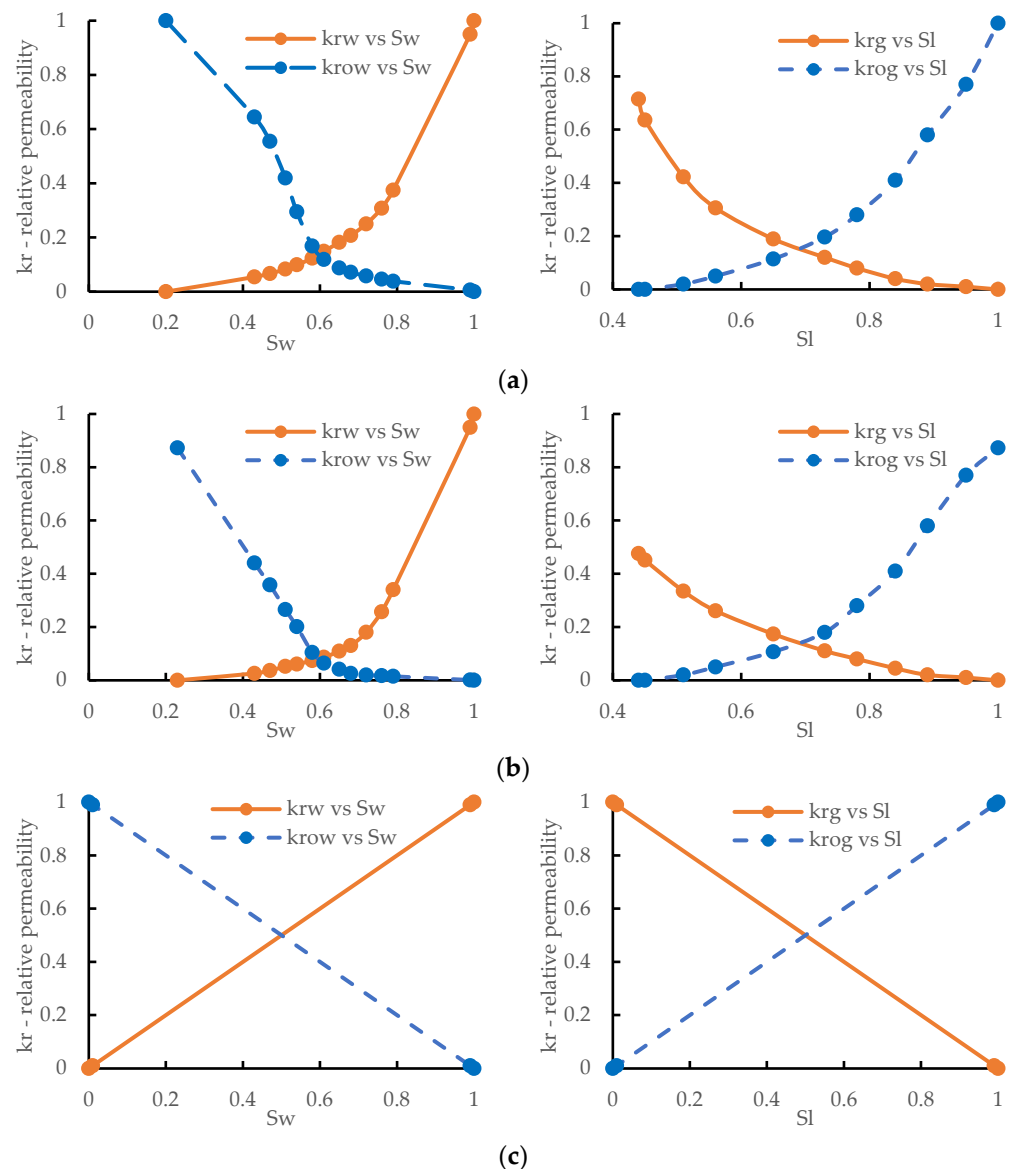
Figure 2. Relative permeability curves of the S91 unit reservoir. (**a**) Caves; (**b**) vugs; (**c**) fractures or faults.

In this study, the geological reverse of the unit was calculated according to the established numerical model. In addition, based on the reservoir types, as well as the characteristics and statistical laws of seismic logging, the porosity, net to gross (NTG), and oil-water saturation were first adjusted, then the geological reverse was fitted according to the actual data. Some fluid production controls were considered to match the oil production index when matching the production history data. First, the relative permeability was modified to match the production history in the entire region. Second, based on seismic data and production data, single-well production fitting was carried out. The numerical simulation model was corrected by adjusting the permeability of adjacent wells and the connectivity with the surrounding reservoirs and water. The best models for dynamic production were established to comprehensively analyze the residual oil distribution with countermeasures to improve exploitation.

(1)　Reverse fitting

The first step of history matching is to fit the geological reverse. The geological reverse of the unit was calculated using the established numerical simulation model. The porosity and oil saturation data were first adjusted based on the reservoir types, then the geological reverse was fitted according to the actual geological reverse. The geological

reverse, calculated using the numerical simulation models, was 1010.5×10^4 rm^3, with a relative error of 0.04% compared to the actual geological reverse of 1010.9×10^4 rm^3, suggesting good reverse fitting.

(2)   History matching production

The liquid and oil velocity data of the S91 unit are shown in Figure 3. The daily data of the liquid and oil production of the simulation results were consistent with the actual production data. Similarly, the responding accumulated production data of the produced liquid and oil were also consistent with the actual well production. The highest well-fitting rate was 90%. Based on the geological data and numerical simulation model results following fitting adjustment, the characteristics and status of the S91 unit can be used to analyze the connectivity relationships of the reservoirs and the adjustment solutions.
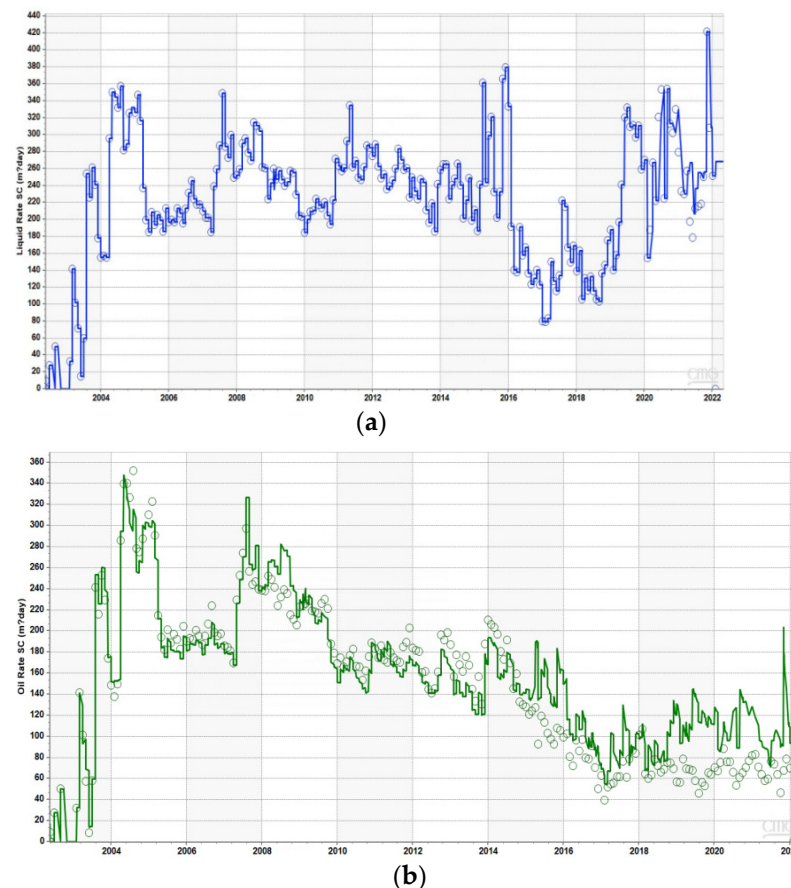

(**a**)

(**b**)

Figure 3. Liquid and oil velocity matching of the S91 unit in the initial model. (**a**) Liquid velocity; (**b**) oil velocity. (the circles represent actual production data, and the lines represent simulation results).

2.3. Residual Oil Distributions between Wells during the Depletion Production Stage

(1)   Residual oil distribution in the control area of a single well

The residual oil distribution types in the control area of a single well in the S91 unit were determined in this study based on the distribution and transport mechanisms of the residual oil, as shown in Figure 4).

The attic residual oil type was located in the fractured-vuggy bodies above the upper oil production layers of the wells. Indeed, residual oil of this type could not be extracted directly. In wells with production layers higher than the oil-water interfaces of the fractured-vuggy bodies, the oil-water interface in the lower part of the fractured-vuggy bodies moved up with oil production. Water flooding occurred in the range of oil production layers of wells, forming the attic residual oil type in the upper part of the fractured-vuggy bodies. For instance, the bottom water was confined slightly in the TK878 well, producing crude

oil in the bottom layer and distributing the residual oil mainly in the upper layer of the well, as shown in Figure 5.
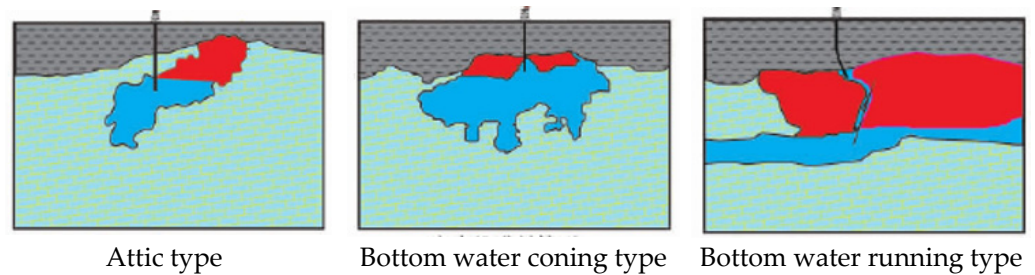

Attic type   Bottom water coning type Bottom water running type

Figure 4. Residual oil distribution types of the control area of a single well.
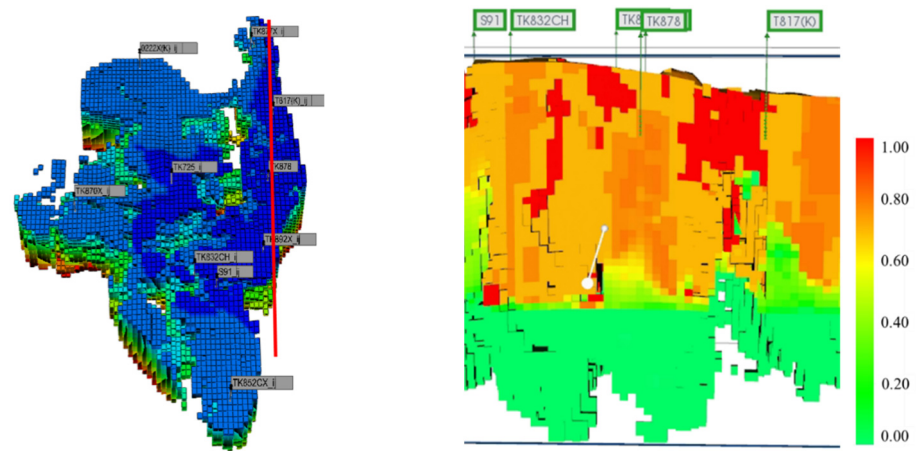

Figure 5. Distribution of the attic residual oil type in the control area of the TK878 well.

The bottom water coning residual oil type was distributed around the well bottom and blocked by the bottom water coning and, consequently, could not be extracted from wells in vugs and fracture reservoirs. For example, the obvious bottom aquifer coning and flooding in the TK725 well contributed to the formation of dispersed residual oil. The residual oil was mainly distributed at the top and sides of the well. In addition, the bottom water contributed to the formation of a large residual oil zone, as shown in Figure 6.
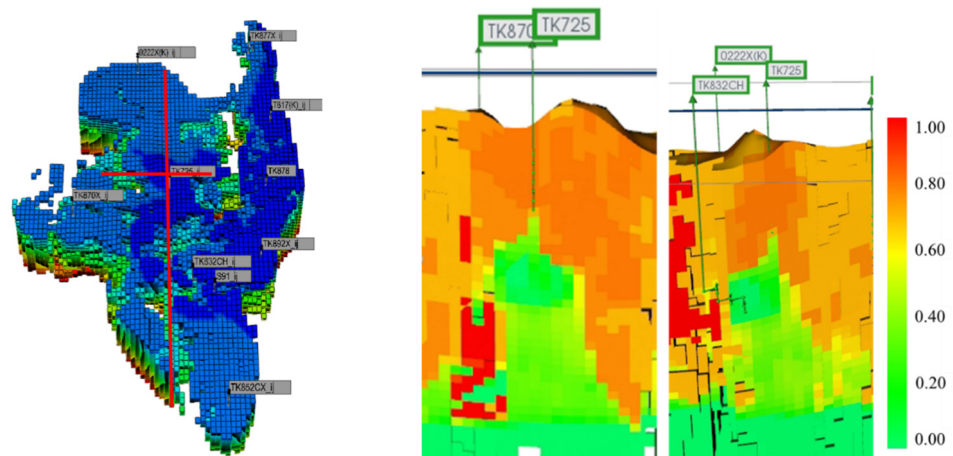

Figure 6. Distribution of the bottom water coning residual oil type in the control area of the TK725 well.

Regarding the bottom aquifer running residual oil type, some fractures connected with the deep bottom water were observed near the well bottom. The deep water flowed rapidly into the well bottom during the production process through the fractures under

certain pressure differences. Because both the water in the fractures ran in with line type and the water was mainly produced after oil water flooding, a high residual oil amount was blocked by the bottom aquifer in the surrounding zones of the oil well and, consequently, could not be extracted directly. For instance, fractures with high angles in the reservoirs across the S91 resulted in high water flows, explaining the distribution of the residual oil around and in the upper part of the well, as shown in Figure 7.
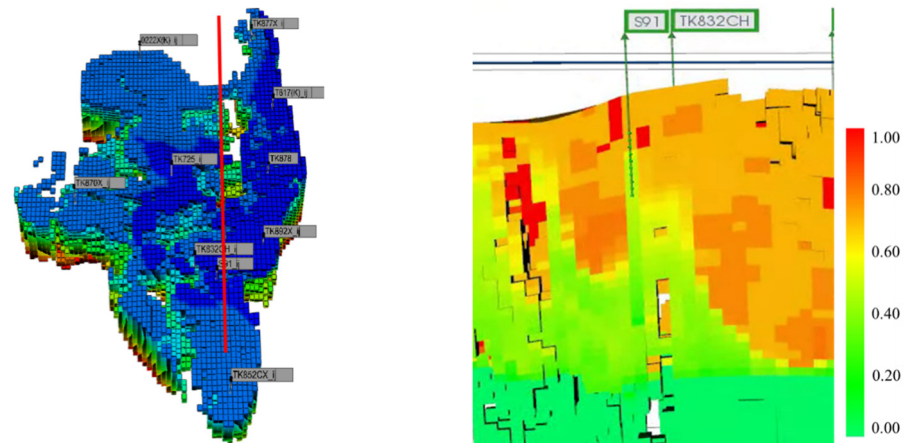

Figure 7. Distribution of bottom water running type in the control area of the S91 well.

(2)   Residual oil distribution between oil wells

As shown in Figure 8, the crude oil in the connected reservoirs between S91 and TK852X was produced effectively. In partial reservoirs between wells (as in the top ones), crude oil was not produced effectively due to isolation or poor connectivity. Whereas in the upper reservoirs between oil wells, a lumpy residual oil distribution was formed. The reverse residual oil was abundant in the reservoirs between wells S91-TK832CH, as well as in the lower and upper layers. In addition, there was a certain amount of residual oil around S91, TK832CH, and TK852CX.
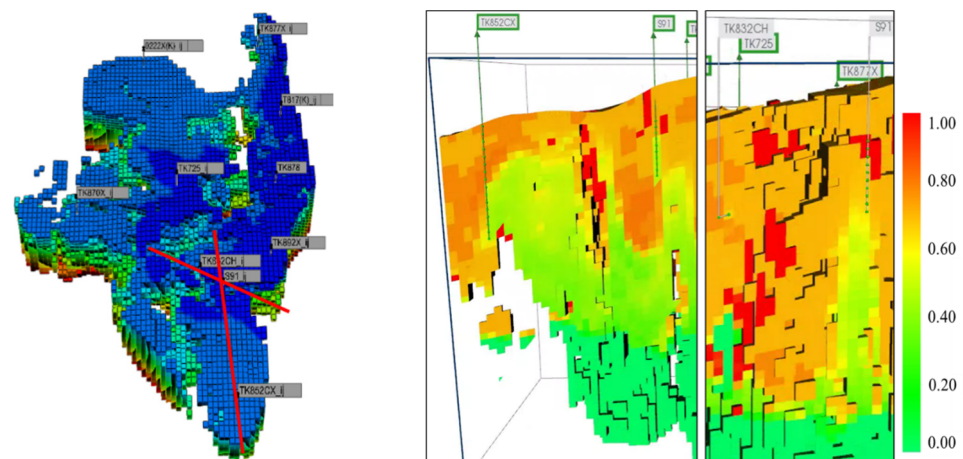

Figure 8. Distribution of residual oil between S91, TK832CH, and TK852CX.

As shown in Figure 9, the water saturation characteristic in the bottom reservoir is a single peak, the same as the large-scale physical experiment [37], and the residual oil between T817(K) and TK877(X) was distributed in the fault areas of the reservoirs, as well as in the upper part around the TK877X well. The reverse residual oil in areas between T817(K), TK878, and TK892X was abundant, of which TK878 and TK892X exhibited good production capacity.
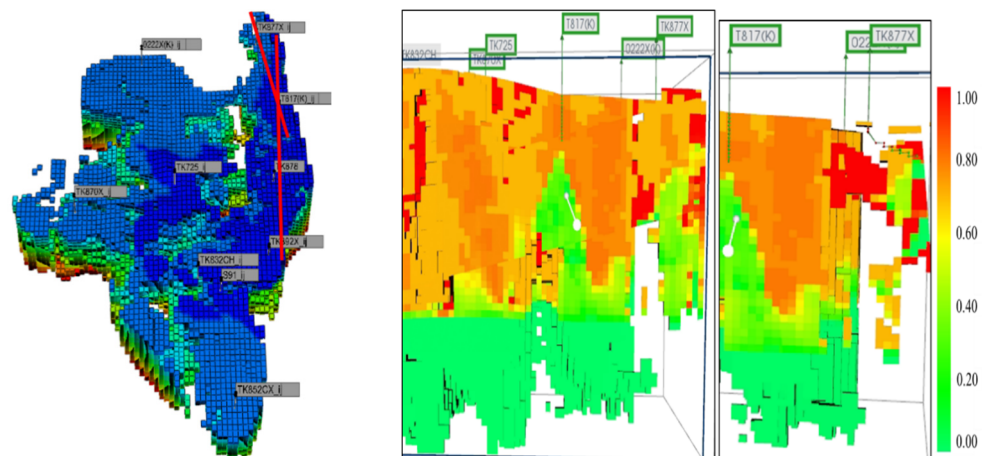
Figure 9. Distribution of residual oil between T817(K), TK878, and TK892X.

As shown in Figure 10, residual oil between TK725 and TK870X was mainly distributed in the middle and upper areas of the reservoirs. However, TK725 exhibited a poor residual oil production capacity due to water flooding. Water flooding occurred mainly in the TK725-0222X(K) section, explaining the high amounts of residual oil reverse in the areas between wells.
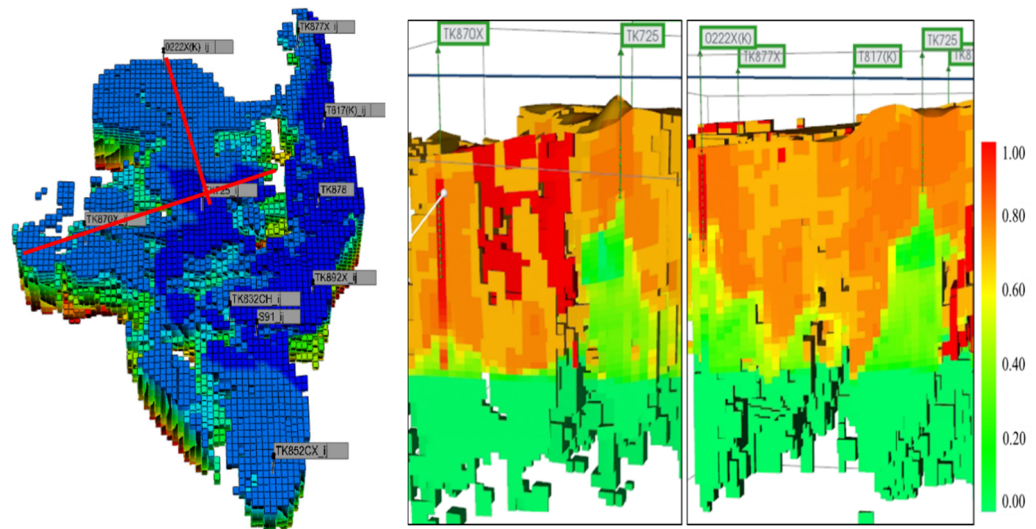

Figure 10. Distribution of residual oil between TL725 and TK870X.

3. Distribution of Residual Oil during the Water Flooding Stage

The flow and migration patterns of the injected water in reservoirs were analyzed in this study based on the simulation results obtained in the S91 unit during the water flooding stage. In addition, the production and distribution status of residual oil was obtained based on the connection relationships of the injected water, obtained using a streamline analysis, a method that is different from other research works [33,36]. According to the obtained results, three residual oil distribution modes during the water flooding stage were identified, namely sweeping the middle between wells, bottom water connection and circulation, and oil separation through high-permeability channels. It should be noted that the analysis of the remaining oil distribution in this work is dynamic analysis on a block-scale [9,34].

3.1. Sweeping the Middle between Wells

By simulating the streamline of the injected water, the flow direction of the injected water in the TK832CH well can be shown as in Figure 11. The simulation results indicated

an occurrence of bottom water coning in the TK832CH well. In addition, the injected water in the TK832CH well was produced through the connection of the bottom water line from three wells, namely S91, TK870X, and TK892X.
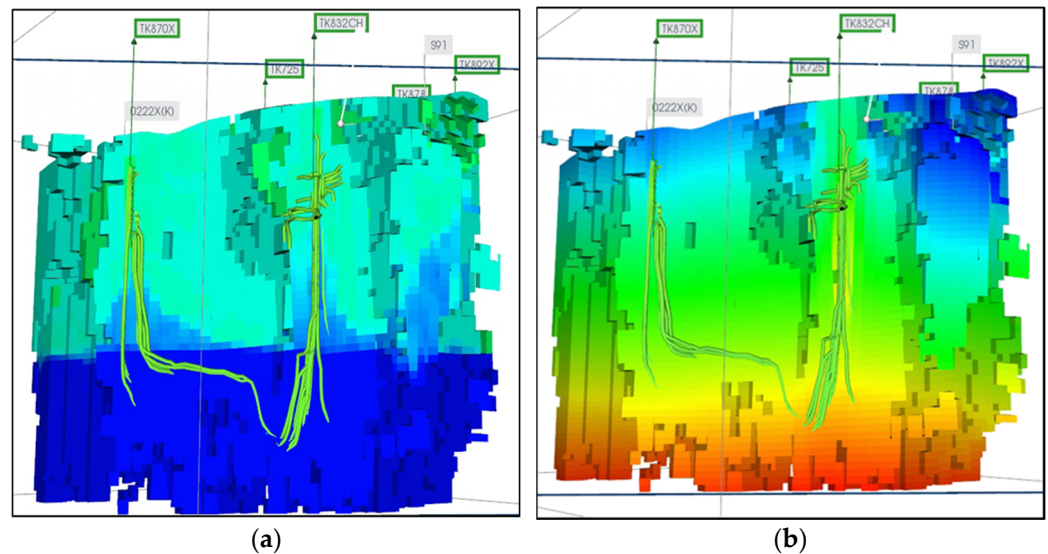

Figure 11. Water and pressure distributions in the TK832CH well. (**a**) Water distribution; (**b**) pressure distribution.

Through the streamline analysis of the injected water, the injected water in the S91 well was shown to flow totally into the TK852CX well. According to the reservoir pressure distribution, as shown in Figure 12, the pressure in the TK852CX well area was low, which was beneficial to the injected water flow from S91 to TK852CX. In addition, the streamline analysis demonstrated good connectivity between the S91-TK852CX wells. Therefore, the injected water in the S91 well could effectively produce residual oil in the zones located between the S91-TK852CX wells.
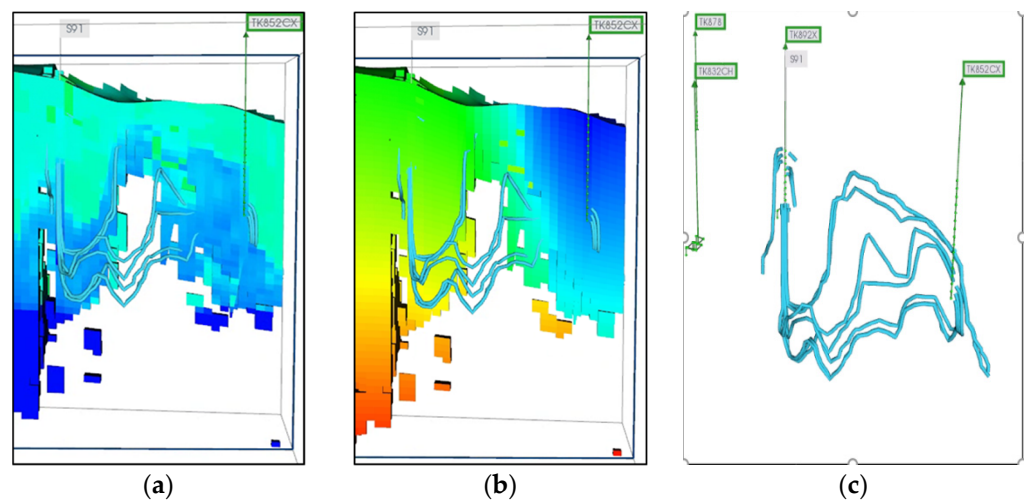

Figure 12. Water distribution, pressure distribution, and streamline of the injected water in the S91 well. (**a**) Water distribution; (**b**) pressure distribution; (**c**) streamline of the injected water.

According to the TK852CX well data, reservoirs surrounding TK852CX were obviously developed, exhibiting certain connectivity with the external reservoirs. Therefore, the injected water in the TK852CX well would also flow to the external area of the unit. In addition, the TK852CX well was located in the low-lying area of the unit, explaining the extension of the flow line of the injected water in TK852CX outside the unit, as shown in Figure 13.
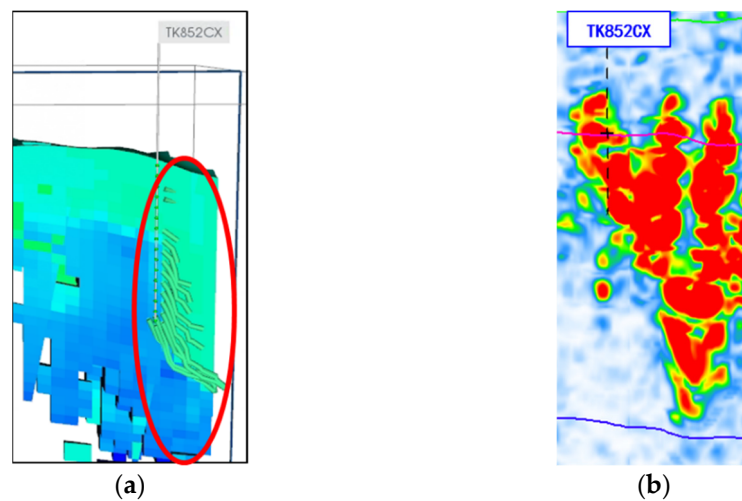
(**a**)

(**b**)

Figure 13. Water and pressure distributions in the TK852CX well. (**a**) Water distribution; (**b**) pressure distribution.

According to the above analysis, the injected water in the TK832CH well flowed into the S91 and TK852CX wells through the bottom reservoir, suggesting good connectivity of TK832CH with S91 and TK852CX and consequently resulting in the effective production of residual oil in the areas between wells.

The residual oil distribution between TK832CH, S91, and TK852CX is shown in Figure 14. The synergistic effect of the injected and bottom water substantially enhanced the crude oil production in the bottom layers. Because of the connections of the bottom reservoirs, the injected water in the TK832CH well reached the bottom area of the S91 well through the connected channel of the bottom waterline, enhancing the residual oil production in areas between TK832CH and S91. The injected water further effectively displaced the residual oil to areas between S91 and TK852CX through the connected channel reservoirs. Therefore, residual oil was mainly distributed in the middle reservoir and upper areas between S91 and TK852CX. The production mode of the residual oil was the sweeping of the middle between wells. According to this analysis, the connection channels of the reservoir types is the key factor of this residual oil distribution model, which is consistent with the 3D water flooding experimental results [35].
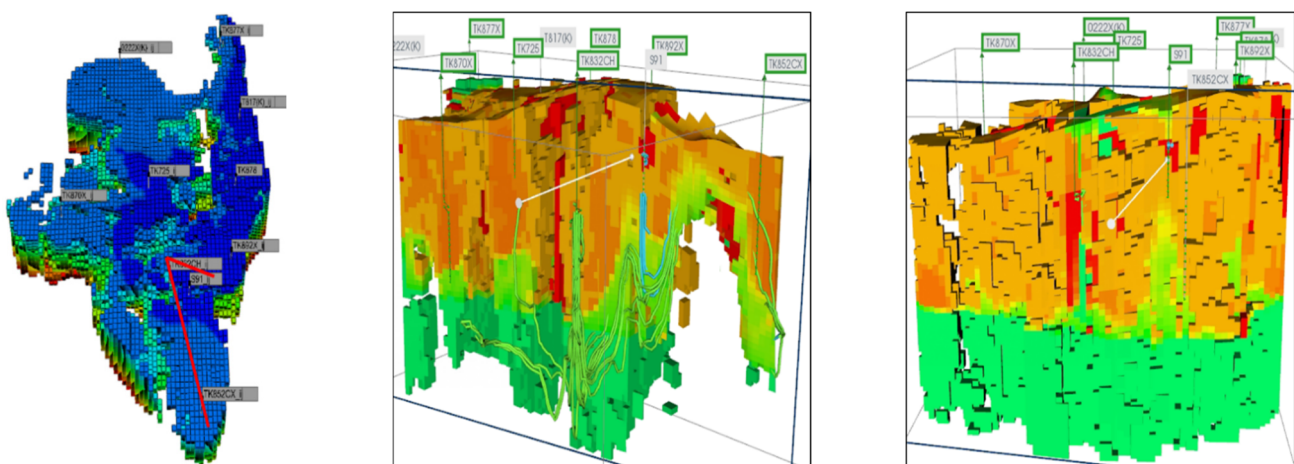

Figure 14. Distribution of residual oil between wells in the TK832CH-S91-TK852CX system.

3.2. Bottom Water Connection and Circulation

As shown in Figure 15, bottom water coning was serious in the TK877X well. In addition, the injected water flowed into the T817(K) well due to the connection of the

bottom reservoirs. According to the reservoir pressure distribution, the bottom pressure of the TK877X well was higher, resulting in an effective driving pressure difference combined with the low-pressure area of the T817(K) well. According to the reservoir development, considerable vugs and fractures were observed in the TK877X-T817(K) areas, suggesting certain connectivity between TK877X and T817(K). In addition, faults near the TK877X well resulted in a vertical flow line across the TK877X well, as shown in Figure 15.
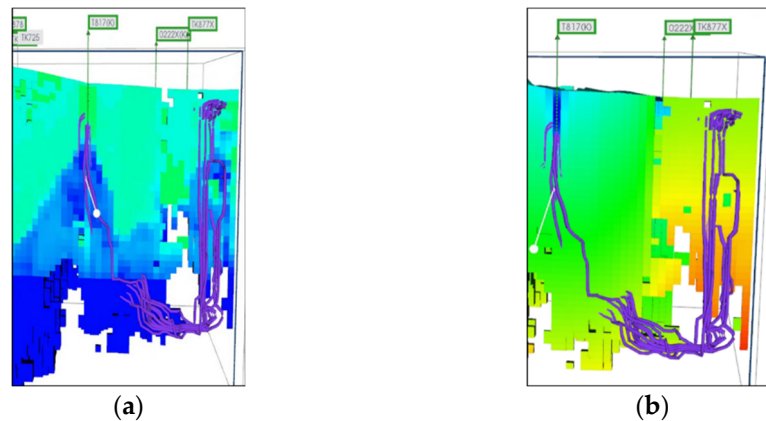

(a)　　　　　　　　　　　　　　　　　　　　　(b)

Figure 15. Water distribution, pressure distribution, and flow line of the injected water around the TK877X well. (**a**) Water distribution; (**b**) pressure distribution.

Figure 16 shows the water distribution and reservoir development around the TK817(K) well. The obtained results revealed complex reservoir development around the TK817(K) well, showing the presence of caves, vugs, and fractures and forming a water cone with the effects of bottom water coning and serious water flooding. In addition, obvious bottom water connections of the TH817(K) well with TK878, TK892X, TK877X, and TK725 were observed due to the flow direction of the injected water. Therefore, the connectivity between TK817(K) and surrounding wells was good.
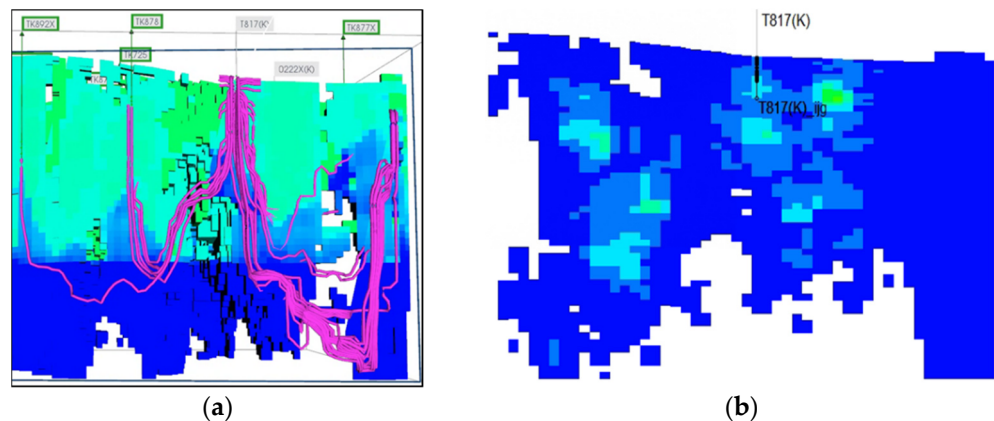

(a)　　　　　　　　　　　　　　　　　　　　　(b)

Figure 16. Water distribution, pressure distribution, and flow line of the injected water around the TK817X well. (**a**) Water distribution; (**b**) pressure distribution.

The analysis results revealed a bottom waterline connection in the T817(K), TK877X, TK878, and TK892XCH wells, as shown in Figure 17. In addition, due to the rising and coning of the bottom water, water flooding occurred in most wells, which deepened the bottom waterline connection between wells.

The produced residual oil consisted mainly of crude oil in the surrounding areas of the wells, as well as in the upper part of the TK877X well, due to serious water flooding in the connection well system. As shown in Figure 18, the actual residual oil was mainly distributed in reservoirs located between the T817(K) and TK877X wells. Due to the high-permeability channels developed in the bottom reservoir, the injected water in the TK817(K)

well reached the bottom water layer, then flowed into the TK877X well through bottom water connections. In addition, high-permeability channels were developed in the bottom reservoir of the TK877X well, distributing residual oil in the reservoirs between T817(K) and TK877X, with low production capacity, associated with the bottom water connection.
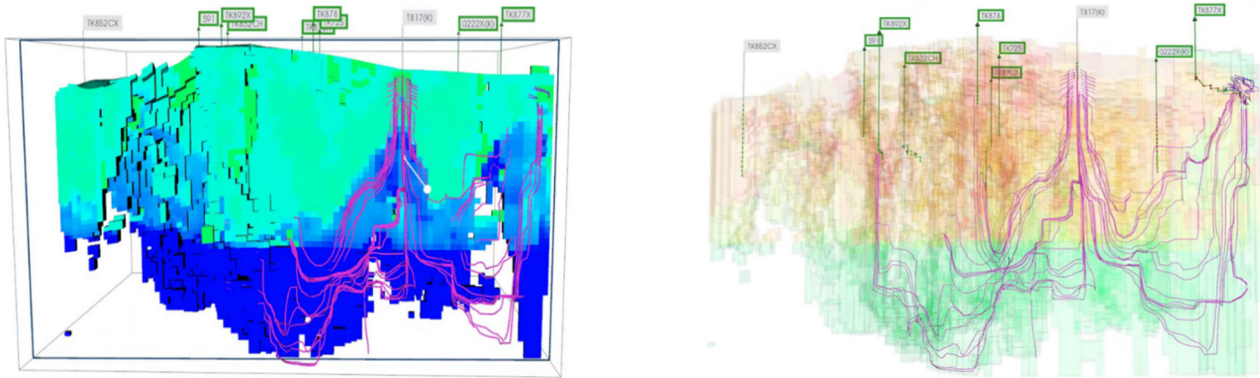

Figure 17. Bottom waterline connection between TK877X, T817(K), TK878, and TK892XCH wells.
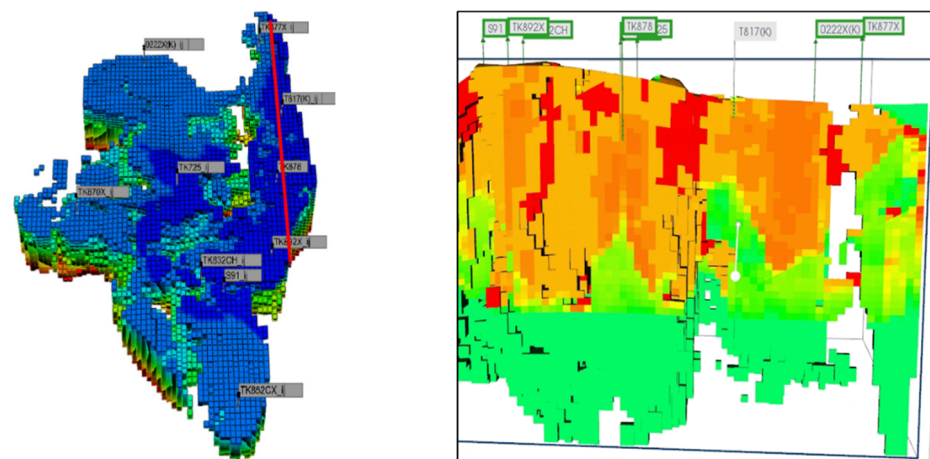

Figure 18. Residual oil distribution between wells in the TK877X-T817(K)-TK878-TK892XCH system.

3.3. Oil Separation through High-Permeability Channels

Figure 19 shows the flowline of the injected water in the TK892X well and the residual oil distribution in areas between the TK892CH and TK832CH wells. It can be seen that the injected water in the TK892X well reached the bottom water layer through the bottom high-permeability channels, then flowed into the S91 and TK832CH wells. Therefore, bottom water connection relations existed between TK892X, S91, and TK832CH. Residual oil production in areas between TK892CH and TK832CH was further analyzed in this study, as shown in Figure 19. The results showed the presence of high-permeability channels in the bottom of the TK892XCH and TK832CH wells. In these wells, the injected water flowed into the bottom water layer through high-permeability channels, resulting in low residual oil production capacities around the wells. Furthermore, the results revealed large residual oil amounts between and around TK892XCH and TK832CH during the water flooding stage. Therefore, the residual oil distribution mode between TK892XCH and TK832CH was oil separation through high-permeability channels.

According to the water saturation distribution around the TK725 well (Figure 20), bottom water coning occurred in the TK725 well, which is explained by the development of vugs in the reservoir in the bottom layer. As shown in Figure 20, the flow direction of the injected water in the TK725 well indicated connections between TK878, T817(K), TK870, and TK832CH through bottom waterline channels.
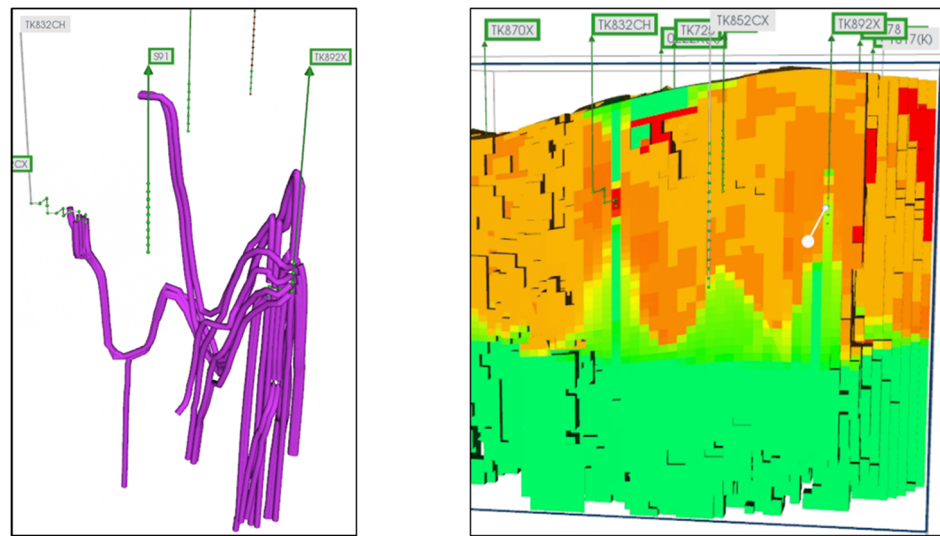
Figure 19. Residual oil distribution in areas between TK892XCH and TK832CH.
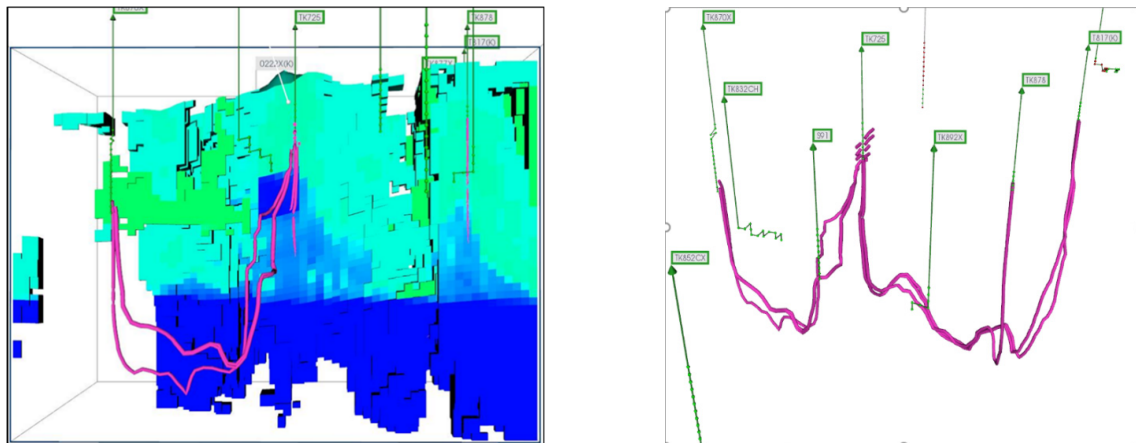

Figure 20. Distribution and flow line of the injected water in areas surrounding the TK725 well.

The residual oil distribution around the TK725 well and between the TK725 and adjacent wells is shown in Figure 21. It can be seen that the bottom crude oil was effectively produced due to the bottom water effect in the area. The residual oil was mainly distributed around the TK725 well and in the upper parts of the reservoirs. Therefore, the residual oil distribution around the TK725 well was oil separation through high-permeability channels.
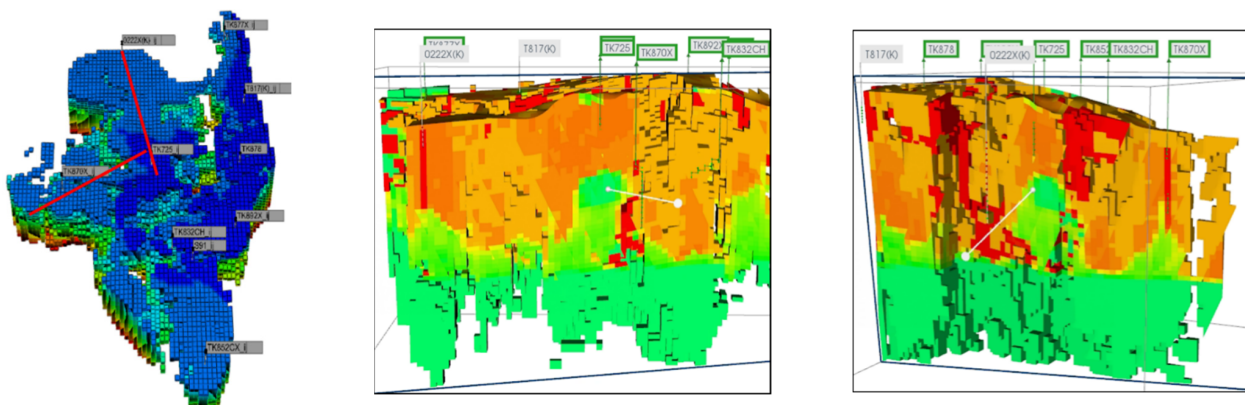

Figure 21. Residual oil distribution between TK725, TK870X, and TH10222X(K).

4. Conclusions

In this study, a reservoir numerical simulation of the S91 unit was performed based on the typical fractured-vuggy fault-karst carbonate reservoir and its porosity and permeability parameters. Derived from history matching, the residual oil distribution laws of the fault-karst reservoirs during the depletion production stage were simulated. In addition, the residual oil distribution laws of the fault-karst reservoirs during the water flooding stage were revealed through the flow line of the injected water in the reservoirs.

(1)   Based on the porosity and permeability parameter of the fault-karst body development, the reservoirs were classified into three types: caves, vugs, and fractures or faults. The numerical simulation models of the fractured-vuggy reservoir of the S91 and TP101 units were established in this study. The results demonstrated good history matching of the dynamic residual oil production, with a fitting accuracy of over 90%.

(2)   During the depletion production stage, the residual oil distribution modes in the well-controlled area of the S91 unit included three residual oil types, namely attic, bottom water coning, and bottom water running type. A substantial bottom water rise was observed due to the development of the reservoir, while a relatively abundant residual oil between wells was observed during the depletion production stage.

(3)   The connection relations of the injected water between wells were investigated in this study at the water flooding stage of the S91 unit using a streamline analysis. In total, three types of residual oil distribution modes during the water flooding stage were identified based on the flow and migration of the injected water in the reservoir, namely sweeping the middle between wells, bottom water connection and circulation, and oil separation through high-permeability channels.

Author Contributions: Conceptualization, B.T.; Methodology, K.R., C.L. and Z.C.; Investigation, L.W.; Writing—original draft, H.L.; Writing—review & editing, C.G.; Supervision, S.W. All authors have read and agreed to the published version of the manuscript.

Data Availability Statement: The data that support the findings of this study are available from the corresponding author upon reasonable request.

Conflicts of Interest: The authors declare that there are no conflict of interest regarding the publication of this manuscript.

References

1.   Ding, Z.; Wang, R.; Chen, F.; Yang, J.; Zhu, Z.; Yang, Z.; Sun, X.; Xian, B.; Li, E.; Shi, T.; et al. Origin, hydrocarbon accumulation and oil-gas enrichment of fault-karst carbonate reservoirs: A case study of Ordovician carbonate reservoirs in South Tahe area of Halahatang oilfield, Tarim Basin. *Pet. Explor. Dev.* **2020**, *47*, 306–317.

2.   Liu, B.; Qi, L.; Li, Z.; Liu, J.; Huang, C.; Yang, L.; Ma, L.; Gong, W. Spatial characterization and quantitative description technology for ultra-deep fault-karst reservoirs in the Shunbei area. *Acta Pet. Sin.* **2020**, *41*, 412–420.

3.   Zhang, C.; Wu, P.; Li, Z.; Liu, T.; Zhao, L.; Hu, D. Ethanol enhanced anionic surfactant solubility in CO_2 and CO_2 foam stability: MD simulation and experimental investigations. *Fuel* **2020**, *267*, 117162. [CrossRef]

4.   Liu, Y.; Rui, Z. A Storage-Driven CO_2 EOR for Net-zero Emission Target. *Engineering* **2022**, *18*, 79–87. [CrossRef]

5.   Qi, L. Characteristics and inspiration of ultra-deep fault-karst reservoir in the Shunbei area of the Tarim Basin. *China Pet. Explor.* **2020**, *25*, 102–111.

6.   Liu, Y.; Rui, Z.; Yang, T.; Dindoruk, B. Using Propanol as an Additive to CO_2 for Improving CO_2 Utilization and Storage in Oil Reservoirs. *Appl. Energy* **2022**, *311*, 118640. [CrossRef]

7.   Zhang, C.; Li, Z.; Sun, Q.; Wang, P.; Wang, S. CO_2 foam properties and the stabilizing mechanism of sodium bis (2-ethylhexyl) sulfosuccinate and hydrophobic nanoparticle mixtures. *Soft Matter* **2016**, *12*, 946–956. [CrossRef]

8. Li, Y.; Qi, L.; Zhang, S.; Yun, L.; Cao, Z.; Han, J.; You, D.; Xiao, H.; Xiao, C. Characteristics and development mode of the Middle and Lower Ordovician fault-karst reservoir in Shunbei area, Tarim Basin. *Acta Pet. Sin.* **2019**, *40*, 1470–1484.

9. Li, R.; Hu, M.; Pan, R.; Hu, Z. Development characteristics and forming mechanism of Middle Permian fault-karst carbonate reservoirs in the central Sichuan Basin. *China Pet. Explor.* **2019**, *24*, 105–114.

10. Shi, W.; Cheng, J.; Liu, Y.; Gao, M.; Tao, L.; Bai, J.; Zhu, Q. Pressure transient analysis of horizontal wells in multibranched fault-karst carbonate reservoirs: Model and application in SHB oilfield. *J. Pet. Sci. Eng.* **2023**, *220*, 111167. [CrossRef]

11. Zhang, C.; Xi, L.; Wu, P.; Li, Z. A novel system for reducing CO_2-crude oil minimum miscibility pressure with CO_2-soluble surfactants. *Fuel* **2020**, *281*, 118690. [CrossRef]

12. Li, Q.; Li, X.; Tao, T.; Song, Z.; Zhang, J.; Liu, H. Constructing Optimum Injection-Production Well Pattern for Fault-Karst Reservoirs. *Xinjiang Pet. Geol.* **2021**, *42*, 213–217.

13. Cheng, X. Characteristics of Water Breakthrough and Optimization of Production System of Oil Wells Drilled in Ultra-Deep Fault-Karst Reservoirs: A Case Study on Well Z in Shunbei Oilfield, Tarim Basin. *Xinjiang Pet. Geol.* **2021**, *42*, 554–558.

14. Lei, J.; Pan, B.; Guo, Y.; Fan, Y.; Xu, Y.; Zou, N. The temperature distribution model and its application to reservoir depth prediction in fault-karst carbonate reservoirs. *Arab. J. Geosci.* **2020**, *13*, 1–11. [CrossRef]

15. Tang, B.; Geng, C.; Huang, M.; Lu, H.; Ren, K. Research on the Depletion and Recovery Characteristics of Fault-Karst Reservoirs. *Geofluids* **2022**, *2022*, 1105335. [CrossRef]

16. Sun, K.; Liu, H.; Leung, J.; Yang, M.; Wang, J.; Li, X.; Kang, Z.; Zhang, Y. Investigation on water-drive performance of a fault-karst carbonate reservoir under different well patterns and injection-production modes based on 2D visualized physical models. *J. Pet. Sci. Eng.* **2022**, *218*, 110925. [CrossRef]

17. Hu, X.; Zheng, W.; Zhao, X.; Niu, B. Quantitative characterization of deep fault-karst carbonate reservoirs: A case study of the Yuejin block in the Tahe oilfield. *Energy Geosci.* **2023**, *4*, 100153. [CrossRef]

18. Fang, J.; Dong, X.; Li, X.; Zhang, G.; Wu, X. Characteristics and Damage Prevention of Fault-Karst Reservoirs in Shunbei Oilfield. *Xinjiang Pet. Geol.* **2021**, *42*, 201–205.

19. Zhao, H.; Li, B.; Zhou, Y.; Zhang, Q.; Liu, H.; Wang, W.; Wang, X. A connectivity prediction model for fault-karst reservoirs based on high-speed non-Darcy flow. *Acta Pet. Sin.* **2022**, *43*, 1026–1034.

20. Liu, Y.; Zhang, C.; Li, S.; Li, Z. Study of steam heat transfer enhanced by CO_2 and chemical agents: In heavy oil production. *Pet. Sci.* **2022**, *20*, 1030–1034. [CrossRef]

21. Chang, B.; Wang, D.; Liu, Z.; Lu, L.; Jiang, J. An Equivalent Reservoir Description Method for Fault-Karst Carbonate Reservoirs. In *Proceedings of the International Field Exploration and Development Conference*; Springer: Berlin/Heidelberg, Germany, 2021.

22. Wu, J.; Li, Z.; Sun, Y.; Cao, X. Neural network-based prediction of remaining oil distribution and optimization of injection-production parameters. *Editor. Dep. Pet. Geol. Recovery Effic.* **2020**, *27*, 85–93.

23. Liang, T.; Hou, J. Fluids flow behaviors of nitrogen and foam-assisted nitrogen floods in 2D visual fault-karst carbonate reservoir physical models. *Editor. Dep. Pet. Geol. Recovery Effic.* **2021**, *200*, 108286. [CrossRef]

24. Gu, H.; Wang, G.; Yang, M.; Cao, F.; Zheng, S.; Shang, G.; Zhu, L.; Han, D.; Kang, Z.; Zhao, Y.; et al. A method for estimating the drainage depth of oil well in ultra-deep fault-karst reservoirs and its guiding significance to oilfield development. *Acta Pet. Sin.* **2021**, *42*, 1202–1211.

25. Cao, L.; Sun, J.; Zhang, B.; Lu, N.; Xu, Y. Sensitivity analysis of the temperature profile changing law in the production string of a high-pressure high-temperature gas well considering the coupling relation among the gas flow friction, gas properties, temperature, and pressure. *Front. Phys.* **2022**, *10*, 1050229. [CrossRef]

26. Wei, C.; Cheng, S.; Chen, G.; Shi, W.; Wu, J.; Wang, Y.; Yu, H. Parameters evaluation of fault-karst carbonate reservoirs with vertical beads-on-string structure based on bottom-hole pressure: Case studies in Shunbei Oilfield, Tarim Basin of Northwestern China. *Oil Gas Sci. Technol.* **2021**, *76*, 59. [CrossRef]

27. Wei, C.; Cheng, S.; Wang, Y.; Shang, R.; Zhu, L.; Yu, H. Pressure Transient Analysis of Wells in the Fault-Karst Carbonate Reservoirs with Vertical Beads-on-String Structure: Case Studies in Shunbei Oilfield, Tarim Basin of Northwestern China. In *Proceedings of the SPE Annual Technical Conference and Exhibition*; OnePetro: Richardson, TX, USA, 2021.

28. Cao, P.; Chang, S.; Zhu, Y.; Shen, J.; Qiao, Z.; Shao, G.; Sun, X. New method for characterizing internal structure of fault-karst reservoirs and analysis on acidizing fracturing effect: A case study in HLHT oilfield, Tarim Basin, NW China. *Lithosphere* **2021**, *2021*, 6784641. [CrossRef]

29. Cao, L.; Sun, J.; Liu, J.; Liu, J. Experiment and Application of Wax Deposition in Dabei Deep Condensate Gas Wells with High Pressure. *Energies* **2022**, *15*, 6200. [CrossRef]

30. Tang, H.; He, J.; Rong, Y.; Li, X. Study on water drive law and characteristics of remaining oil distribution of typical fault-karst in fault-karst reservoirs, Tahe Oilfield. *Pet. Geol. Recovery Effic.* **2018**, *25*, 95–100.

31. Wang, J.; Liu, H.; Xu, J.; Zhang, H. Formation mechanism and distribution law of remaining oil in fracture-cavity reservoirs. *Pet. Explor. Dev.* **2012**, *39*, 585–590. [CrossRef]

32. Wang, J.; Qi, X.; Liu, H.; Yang, M.; Li, X.; Liu, H.; Zhang, T. Mechanisms of remaining oil formation by water flooding and enhanced oil recovery by reversing water injection in fractured-vuggy reservoirs. *Pet. Explor. Dev.* **2022**, *49*, 1110–1125. [CrossRef]

33. Zheng, S.; Yang, M.; Kang, Z.; Liu, Z.; Long, X.; Liu, K.; Li, X.; Zhang, S. Controlling factors of remaining oil distribution after water flooding and enhanced oil recovery methods for fracture-cavity carbonate reservoirs in Tahe Oilfield. *Pet. Explor. Dev.* **2019**, *46*, 746–754. [CrossRef]

34. Rong, Y.; Zhao, J.; Lu, X.; Li, X.; Li, X. Remaining oil distribution patterns and potential-tapping countermeasures in carbonate fracture-cavity reservoir. *Acta Pet. Sin.* **2014**, *35*, 1138–1146.
35. Li, S.; Liu, Y.; Xue, L.; Yang, L.; Yuan, Z.; Jian, C. An investigation on water flooding performance and pattern of porous carbonate reservoirs with bottom water. *J. Pet. Sci. Eng.* **2021**, *200*, 108353. [CrossRef]
36. Yang, M.; Li, X.; Tan, T.; Li, Q.; Liu, H.; Zhang, Y. Remaining oil distribution and potential tapping measures for palaeo-subterranean river reservoirs:A case study of TK440 well area in Tahe Oilfield. *Reserv. Eval. Dev.* **2020**, *10*, 43–48.
37. Liu, Y.; Liu, Y.; Zhang, Q.; Zheng, W.; Jian, C.; Li, G.; Xue, Y. Large-scale physical simulation experimental study on thick carbonate reservoirs. *Pet. Geol. Recovery Effic.* **2020**, *27*, 117–125.
38. Liu, P.; Lin, J.; Tang, B.; Ren, K.; Huang, M.; Geng, C. Residual Oil Distribution Pattern in a Fault-Solution Carbonate Reservoir and Countermeasures to Improve Oil Development Effectiveness. *Geofluids* **2022**, *2022*, 2147200. [CrossRef]